Elastic and inelastic neutron scattering experiments under high pressure in frustrated antiferromagnet $CuFeO_2$

Noriki Terada[1], Dmitry D. Kyalyavin[2], Pascal Manuel[2], Shinichiro Asai[3], Takatsugu Masuda[3], Hiraku Saito[3], Taro Nakajima[3,4], and Toyotaka Osakabe[5]

[1]*National Institute for Materials Science, Sengen 1-2-1, Tsukuba, Ibaraki 305-0047, Japan*

[2]*ISIS facility, STFC Rutherford Appleton Laboratory, Chilton, Didcot, Oxfordshire, OX11 0QX, United Kingdom*

[3]*Institute for Solid State Physics, The University of Tokyo, Kashiwa 277-8581, Japan*

[4]*RIKEN Center for Emergent Matter Science (CEMS), Wako, 351-0198, Japan and*

[5]*Japan Atomic Energy Agency, Tokai, Ibaraki 319-1195, Japan*

(Dated: June 23, 2024)

Abstract

The frustrated antiferromagnet $CuFeO_2$ exhibits pressure-induced complex magnetic phase transitions from the commensurate collinear (CM1) phase to several incommensurate noncollinear phases. To study the effect of high pressure on magnetic interactions, we performed neutron diffraction and inelastic neutron scattering experiments under high-pressure conditions. With increasing pressure, the CM1 ground state becomes less stable against application of a magnetic field even below the critical pressure ($P \leq 3$ GPa), as proved by the significant reduction in the critical magnetic field from H_{c1} =7.5 T to 4.5 T at 2.1 GPa. Additionally, the energy gap in the spin-wave dispersion relation is reduced from 1.0 to 0.88 meV by the application of a pressure of $P = 2.1$ GPa. Comparing the experimental results with spin-wave calculations revealed that the change in the spin-wave excitation can be explained by the reduction in either the uniaxial anisotropy term or the degree of separation in the nearest-neighbor exchange interactions.

PACS numbers: 75.80.+q, 75.50.Ee, 75.25.+z, 77.80.-e

I. INTRODUCTION

In frustrated magnets, as a consequence of competing exchange interactions caused by geometric lattice patterns (triangular, Kagomé, pyrochlore lattices) and additional special interactions (Dzyaloshinskii–Moriya (DM), biquadratic exchange interactions), exotic magnetic ground states often emerge, such as spiral-order[1,2], spin ice[3,4], skyrmions[5,6], and spin liquids[7,8]. Furthermore, when frustrated spins are strongly coupled to the crystal lattice through inverse effects, such as exchange striction[9] and the inverse DM effect[10,11], novel physical phenomena can occur, such as magnetoelectric multiferroic properties[12,13] and magnetization plateaus[14,15]. Because the magnetic ground state in a frustrated magnetic system is nearly degenerated by the others, it can be renewed by a small change in the spin Hamiltonian parameters. High pressure (hydrostatic and uniaxial) and chemical substitution can be used to modify these parameters, leading to significant changes in the magnetic ground state by disturbing the delicate balance of competing interactions in frustrated magnetic systems.

Recently, pressure-induced magnetic phase transitions have been reported in triangular-lattice antiferromagnetic $CuFeO_2$ (CFO)[16,17]. CFO is a delafossite-family compound (ABO_2, A =Cu, Ag, Pd, Pt, B = Fe, Cr)[18–20] and has been extensively studied as a typical frustrated magnet. At the ambient pressure, the commensurate (CM) collinear $\uparrow\uparrow\downarrow\downarrow$ magnetic structure is realized (magnetic propagation vector $\boldsymbol{k} = (0, \frac{1}{2}, \frac{1}{2})$ in the monoclinic setting shown in Fig. 1) as the magnetic ground state below $T = 11$ K in the CM1 phase[21,22]. In the intermediate temperature range of 11 K $\leq T \leq$ 14 K, a sinusoidally modulated magnetic structure with incommensurate (ICM) $\boldsymbol{k} = (0, q, \frac{1}{2})$ is stabilized in the ICM1 phase[23]. As indicated by the temperature–pressure phase diagram in Fig. 2, application of pressure above P =2.5 GPa drives the magnetic phase transition to the ICM noncollinear spiral state (ICM2) with $\boldsymbol{k} = (0, q, \frac{1}{2}; q \sim 0.4)$[16,17]. Spiral magnetic ordering—called proper screw—in the ICM2 phase is identical to that observed in the ground state of the magnetic-field-induced phase or chemical-substitution-induced phase[24,25]. When the pressure is further increased from the ICM2 phase above P =4.0 GPa, another ICM noncollinear phase (ICM3) with $\boldsymbol{k} = (q_a, q_b, q_c; q_a \sim 0, q_b \sim 0.34, q_c \sim 0.42)$ is induced, which is called a general spiral[16,17]. For the intermediate temperature range between these ground states and the paramagnetic phase, the ICM spin-density-wave ordering (ICM1) for lower pressures changes to another

noncollinear state (ICM4) above $P \sim$3 GPa[17].

In previous studies on the ambient pressure conditions in CFO, magnetic interaction parameters, including exchange constants and anisotropies, were determined via inelastic neutron scattering (INS) and electron spin resonance (ESR) experiments[26–28]. However, the effect of pressure on the magnetic interactions in CFO has not been investigated. Therefore, the origin of pressure-induced phase transitions is not yet understood. In the present study, to investigate the pressure-induced phase transitions in CFO, we examined the stability of the pressure-induced ICM states against an external magnetic field and the pressure change in spin-wave excitation spectra through elastic and INS experiments.

II. EXPERIMENTAL DETAILS

A single-crystal crystal sample was grown using the optical floating-zone method. Neutron diffraction (ND) experiments were performed using the cold neutron time-of-flight diffractometer WISH[29] at the ISIS Facility in the U.K. To apply a hydrostatic pressure lower than $P = 2.5$ GPa, we used a clamp cell with a diameter of ϕ20 mm and a length of 55 mm, which was made of NiCrAl and CuBe alloys with thicknesses of 3.0 and 4.5 mm, respectively (ElectroLAB). A single crystal with a volume of approximately 20 mm^3 was mounted in a Teflon capsule with a ϕ4.0-mm inner diameter, and the sample was filled with a glycerin pressure transmitting medium. The pressure was calibrated by the NH_4F structure phase transition points at room temperature. The hexagonal c axis (c^* axis in the monoclinic setting) was parallel to the external magnetic field generated by the vertical-field cryomagnet (up to 13.4 T).

For ND experiments in the upper pressure range, i.e., $P = 3.0$ to 4.1 GPa, we used a hybrid anvil-type high-pressure cell[30–32]. The sample was cut into a plate-like shape with dimensions of approximately 0.6 $\times$ 0.5 $\times$ 0.2 mm^3. We used a sapphire crystal and WC alloy for the pair of anvils and an aluminum alloy (Al2017) for the gasket. We also used glycerin as the pressure transmitting medium. Pressure values were determined using the ruby fluorescence method at room temperature. The pressure cell was inserted into a vertical-field superconducting magnet (up to 10 T) such that the hexagonal c axis was vertical.

For the INS experiment, we used the triple-axis neutron spectrometers HER and PONTA

at the reactor source neutron facility JRR-3 in Tokai, Japan. In these experiments, we used the same clamp cell that was employed for the ND experiments and a 38-mm^3-volume CFO single crystal. A deuterated glycerin pressure transmitting medium was used for the INS experiments. The pressure cell was set up and calibrated using the same procedures employed in the ND experiments. To measure the spin-wave excitation spectra in the hexagonal (H, H, L) zone (monoclinic $(0, K, L)$ zone), the sample was mounted such that the hexagonal $[1\bar{1}0]$ axis (monoclinic a axis) was vertical. A closed-cycle refrigerator was used to cool the samples. We employed the constant-E_f mode (E_f represents the energy of scattered neutrons) with the fixed E_f=2.5 meV and E_f=3.64 meV for the cold neutron experiment with HER and E_f=14.7 meV for the thermal neutron experiment with PONTA. The instrumental E resolutions were 0.08 meV for E_f=2.5 meV (0.12 meV for E_f=3.64 meV) for HER and 0.94 meV for PONTA at the elastic position.

III. EXPERIMENTAL RESULTS

A. Elastic neutron scattering

As shown in the phase diagram as a function of the magnetic field (along the hexagonal c axis) at the ambient pressure in Fig. 2, the spin-flop phase transition occurs from CM1 to the ICM noncollinear spiral state (ICM2) at $H_{c1} = 7.5$ T. Another CM collinear state, i.e., $\uparrow\uparrow\uparrow\downarrow\downarrow$ (CM2), was induced at $H_{c2} = 12.5$ T[33–35]. Because the critical phase transitions H_{c1} and H_{c2} are sensitive to changes in exchange interactions and anisotropies in the CFO, we investigated the effect of pressure on the phase transitions via ND experiments. Although further high-field phases exist, such as the $\uparrow\uparrow\downarrow$ phase (20 T $\leq H_{||c} \leq$ 34 T) and the canted $\uparrow\uparrow\downarrow$ phase (34 T $\leq H_{||c} \leq$ 53 T)[28,36], we could not investigate the pressure effect on these phases in the present study, because of experimental limitations.

As shown in Fig. 3(a), the magnetic neutron Bragg peaks were observed on $\boldsymbol{Q} = (1, -0.5, -0.5)$ in the monoclinic setting ($\boldsymbol{Q} = (-0.25, -0.5, -0.5)$ in the hexagonal setting), at $T = 2$ K and $H_{||c} = 0$ T. Hereafter, we use a monoclinic setting unless specified otherwise. The reciprocal lattice maps with the magnetic Bragg positions for the monoclinic bases are presented in Supplementary Fig. 1.[37] The Bragg peak position can be expressed as the satellite reflection from the reciprocal lattice position at

$\boldsymbol{\tau} = (1, -1, -1)$ using the CM $\boldsymbol{k}_{CM1} = (0, 0.5, 0.5)$ characteristic of the CM1 phase, i.e., $\boldsymbol{Q} = \boldsymbol{\tau} + \boldsymbol{k}$. In addition, two low-intensity signals were observed at the two ICM positions $\boldsymbol{Q} = (1, -0.6, -0.5)$ and $(1, -0.4, -0.5)$ even without a magnetic field, which can be expressed as $\boldsymbol{Q} = (1, -1, -1) + \boldsymbol{k}_{ICM2}$ and $\boldsymbol{Q} = (1, 0, 0) - \boldsymbol{k}_{ICM2}$ with $\boldsymbol{k}_{ICM2} = (0, q, 0.5)$ having the $q \sim 0.4$ characteristic of the ICM2 spiral phase. The crystal lattice in the CM1 and ICM2 phases is distorted from the parent rhombohedral space group $R\bar{3}m$ to a monoclinic symmetry because of the exchange-striction mechanism described in previous X-ray diffraction studies[38–41].

With increasing $H_{||c}$ at $T = 1.5$ K and $P = 2.1$ GPa, the CM peak disappeared, and the intensities of the ICM peaks were increased at $H_{||c} = 4.5$ T, as shown in Figs. 3(b), 3(c), and 3(e). This result corresponds to the transition from the CM1 phase to the ICM2 phase at H_{c1}. The critical field is significantly reduced by the application of a 2.1 GPa pressure from the ambient pressure of 7.5 T. The $\boldsymbol{k}$ vector component q depends on $H_{||c}$ in the ICM2 phase, which changes from 0.405 at 5 T to 0.390 at 12 T for $P = 2.1$ GPa. The q value at $P = 2.1$ GPa is slightly different from that at ambient-pressure values of 0.415 at 7.5 T and 0.402 at 12.5 T. With a further increase $H_{||c}$, the magnetic Bragg reflections corresponding to the ICM2 phase disappeared at 13 T, and the intensity at the other CM position of $\boldsymbol{Q} = (1, -0.6, -0.5)$ onsets at this field. The CM position is consistent with that observed for the CM2 phase at the ambient pressure. H_{c2} =12.5 T at $P = 2.1$ GPa, which is almost the same as the critical field at the ambient pressure. Consequently, we found that the first critical field H_{c1} was significantly weakened by the application of pressure, whereas the second critical field H_{c2} was almost independent of the pressure in the CFO.

To investigate the stabilities of the pressure-induced phases of ICM2 and ICM3 against the application of $H_{||c}$, we performed ND experiments with a hybrid anvil-cell for $P = 3.1$ GPa and 4.0 GPa. At $P = 3.1$ GPa, a magnetic Bragg reflection at $\boldsymbol{Q} = (-1, 0.6, 0.5)$ corresponding to ICM2 ordering was observed, as shown in Fig. 4(a). Another satellite peak for the ICM2 phase was observed at $\boldsymbol{Q} = (-1, 0.4, 0.5)$ (not shown). In addition, two Bragg spots were observed at $\boldsymbol{Q} = (-1, 0.66, 0.41)$ and $\boldsymbol{Q} = (-1, 0.66, 0.59)$, which originated from the ICM3 ordering with $\boldsymbol{k}_{ICM3} = (q_a, q_b, q_c)$ with $q_a \sim 0$, $q_b \sim 0.34$, and $q_c \sim 0.41$. The coexistence of the ICM2 and ICM3 phases around $P \sim 3$ GPa was also observed in previous ND experiments[16,17]. When $H_{||c}$ of up to 10 T is applied, the magnetic Bragg intensities are not changed within the experimental accuracy, as shown in Figs. 4(b)

and 4(e).

The temperature dependences of the magnetic reflections corresponding to the ICM2 and ICM3 phases are shown in Figs. 4(f) and 4(g), respectively. The intensity of the Bragg reflection for the ICM2 phase is constant below T =8 K and is increased in the intermediate temperature range of 8–12 K (Fig. 4(f)). This intensity enhancement is attributed to the additional contribution of either the ICM1 phase (sinusoidal spin state) or the ICM4 phase (canted proper screw), owing to the same propagation vector of $\boldsymbol{k} = (0, q, \frac{1}{2}; q \sim 0.4)$ in both the ICM2 and ICM1 (or ICM4) phases. In contrast, the intensity of the ICM3 phase decreases monotonically as the temperature increases from 1.5 K, and the peak disappears at $T = 8$ K (Fig. 4(g)). This indicates a phase transition from ICM3 to ICM4.

At 4.0 GPa, only the reflection of the ICM3 phase was observed (Fig. 4(c)). The intensity of the ICM3 reflection was constant up to 10 T, within the experimental accuracy. The peak position of the ICM3 phase, corresponding to the ICM3 $\boldsymbol{k}$ vector components, did not change with an increase in $H_{||c}$ to 10 T. Consequently, the pressure-induced ICM3 phase is robust against $H_{||c}$ up to 10 T.

The ND experimental results are presented as functions of $H_{||c}$ and the pressure at the lowest temperature in the phase diagram of Fig. 1. The $H_{||c}$-induced phase transition from CM1 to ICM2 at H_{c1} was significantly suppressed by the application of pressure, whereas that from ICM2 to CM2 at H_{c2} was robust against the application of pressure, at least up to $P = 2.1$ GPa. We also observed that the magnetic ordering of the ICM3 phase was not affected by $H_{||c}$ up to 10 T.

B. Inelastic neutron scattering

To directly study the changes in the magnetic interactions in CFO caused by the application of pressure, we investigated the spin-wave dispersion relation at 2.1 GPa via INS experiments. At the ambient pressure, CFO exhibits a spin-wave dispersion relation with double minima at $\boldsymbol{Q} = (0, q, 0.5)$ and $\boldsymbol{Q} = (0, 1 - q, 0.5)$ in the CM1 phase. The energy gap is 1.0 meV at the ambient pressure[26,27]. The INS intensity in the present high-pressure experiment with a clamp cell having a 15-mm thickness (CuBe and NiCrAl alloys) window was approximately 20 times lower than that without the pressure cell, which was normalized to the sample mass. Thus, we focused on measuring the spin-wave spectra at typical

$\boldsymbol{Q}$ positions in the $(0, K, L)$ scattering plane.

A comparison of the INS spectra measured by the HER between the ambient pressure and P =2.1 GPa at T =2.5 K is presented in Fig. 5(a). The energy gap for the energy minimum at the ICM position $\boldsymbol{Q} = (0, 0.42, 0.5)$ is reduced from 1.0 meV at the ambient pressure to 0.88 meV at P =2.1 GPa. The excitation signals above 1.0 meV (double arrows) originate from another magnetic domain contribution that depends on the domain population. Furthermore, the energy around the zone boundary at $\boldsymbol{Q} = (0, 0, 0.5)$ is slightly reduced from 2.51 meV at the ambient pressure to 2.45 meV at $P = 2.1$ GPa. (Figs. 5(b)) We also performed a constant-Q scan at $\boldsymbol{Q} = (0, 0, 2.4)$ at the ambient pressure and $P = 2.1$ GPa using the PONTA spectrometer. No clear differences were observed between the spectra (Supplementary Fig. 2[37]).

IV. DISCUSSION

Considering the ND and INS experimental results, we discuss the effect of pressure on the magnetic interactions in CFO. The spin Hamiltonian for CFO can be expressed as

$$\mathcal{H} = -\frac{1}{2}\sum_{i,j} J_n \boldsymbol{S}_i \cdot \boldsymbol{S}_j - \sum_i D(S_i^z)^2, \tag{1}$$

where J_n and D denote the exchange interaction and uniaxial anisotropy constant, respectively. The crystal structure of CFO is distorted from an equilateral triangular lattice to a scalene triangular lattice in the CM1 phase because of exchange restriction[38–41]. In previous INS and ESR studies at the ambient pressure, inequivalent exchange interactions due to lattice distortion were essential for explaining the spin-wave dispersion relation of CFO[27,28]. Additionally, in other theoretical studies, researchers considered the separation of exchange interactions due to lattice distortion in CFO[43,44]. The exchange paths considered in the present study for the scalene triangular lattice are illustrated in Fig. 6(a). The nearest-neighbor interaction J_1 in the equeary triangular lattice is separated into one weak (J_{11}) and two strong (J_{12} and J_{13}) exchange interactions. However, for the second neighbor J_2, third neighbor J_3, and interplane bond J_z, the lattice distortion effect is negligible. In this study, we considered the exchange separation due to lattice distortion only for the nearest-neighbor interaction J_1. Thus, we considered seven magnetic interaction parameters: J_{11}, J_{12}, J_{13}, J_2, J_3, J_z, and the uniaxial anisotropy parameter D. (Weak in-plane anisotropy

TABLE I: Spin Hamiltonian parameters (in meV). The exchange parameters at 0 GPa were taken from Ref.[27].

	$J_{11}S$	$J_{12}S$	$J_{13}S$	J_2S	J_3S	J_zS	DS	E_g	E_{zb}
0 GPa	−0.150	−0.455	−0.422	−0.10	−0.33	−0.19	0.20	1.01	2.40
(a)	−0.150	−0.455	−0.422	−0.10	−0.33	−0.19	0.16	0.89	2.34
(b)	−0.150	−0.420	−0.401	−0.10	−0.33	−0.19	0.20	0.89	2.34
(c)	−0.150	−0.455	−0.422	−0.12	−0.33	−0.19	0.20	0.90	2.41
(d)	−0.150	−0.455	−0.422	−0.10	−0.39	−0.19	0.20	0.90	2.49
(e)	−0.150	−0.455	−0.422	−0.10	−0.33	−0.17	0.20	1.04	2.31
(f)	−0.200	−0.455	−0.422	−0.10	−0.33	−0.19	0.20	1.01	2.40

interactions were ignored.)

Owing to the limited number of experimental results for the present INS under high-pressure conditions, it was not possible to determine all magnetic interactions under high-pressure conditions simultaneously. Therefore, we discuss the influence of pressure on the magnetic interactions by comparing the calculated spin-wave dispersion relations based on the modified individual magnetic interaction parameters with the experimental results. Spin-wave calculations were conducted using the Holstein–Primakoff transformation method described in a previous report[27].

We calculated the spin-wave dispersion relation using the spin Hamiltonian parameters at the ambient pressure based on a previous study[27]. These parameters are presented in Table 1. As mentioned previously, the dispersion relation has two minima with an energy gap of 1 meV, as indicated by the solid lines in Figs. 6(b). In the experiment, the energy gap (E_g) at $\boldsymbol{Q} = (0, 0.42, 0.5)$ was reduced to 0.88 meV. There are many possibilities for reproducing the reduction in the energy gap, as summarized in Table 1. For case (a) in Table 1, when we change the anisotropy parameter D from -0.20 to -0.16 meV, the calculated energy gap is reduced to the experimental value at $P = 2.1$ GPa. In addition, by changing the ratio between the nearest-neighbor antiferromagnetic exchange interactions for case (b), i.e., the weak J_{11} and strong J_{12} (J_{13}) interactions, we can reproduce the energy gap at $P = 2.1$ GPa. In both cases (a) and (b), the energy at the zone boundary (E_{zb}) $\boldsymbol{Q} = (0, 0, 0.5)$ is slightly lower, which is consistent with the experimental results. However, when the

other parameters are changed, the second-nearest neighbor J_2, the third neighbor J_3, E_g is reduced, but E_{zb} is not reduced, as shown in Table 1 and Supplementary Fig. 3(a)[37]. Changing the interplane interaction J_z and J_{11} does not reproduce the reduction in E_g as in cases (e) and (f), respectively (Supplementary Fig. 3(b)[37]). Therefore, we found that the most probable magnetic interaction parameters to be changed by the application of pressure were either the anisotropy parameter D or the nearest-neighbor exchange interactions J_{12} and J_{13}.

Let us discuss the effect of pressure on the phase stability against $H_{||c}$ and magnetic-field-induced phase transitions in CFO. In the ND experiment, we observed a significant change in the critical field H_{c1} between the collinear CM1 phase and the proper screw ICM2 phase, as illustrated in Figs. 7(a) and 7(b). The energy values per spin for the collinear state for the CM1 and ICM2 phases at zero temperature are given as follows:

$$\begin{aligned} E_{\mathrm{CM1}} &= -S^2(J_{11} - (J_{12} + J_{13}) + A) - DS_z^2 \\ E_{\mathrm{ICM2}} &= -S^2(\alpha J_{11} + \beta(J_{12} + J_{13}) + B) - \frac{1}{2}DS_z^2, \end{aligned}$$

where A and B are the exchange energy terms associated with J_2, J_3, and J_z, α is close to 1 because of the phase shift δ in Fig. 7(b) nearly equal to πq[24,25], and β is $\cos(2\pi q)$ with $q \sim 0.42$. When either the anisotropy parameter D or $(J_{12} + J_{13})$ is reduced, as expected from the INS experiment, the degree of energy increase in E_{CM1} exceeds that in E_{ICM2}. This implies that the CM1 magnetic state becomes more unstable than the ICM2 state with a reduction in D or $(J_{12} + J_{13})$, which is consistent with the significant decrease in the critical field of the phase transition from CM1 to ICM2 observed in the present ND experiment. Similar findings for the stability of the ICM2 phase have been reported in the case of chemical substitution in Ga-doped $CuFe_{1-x}Ga_xO_2$[45]. We did not understand the stability of the higher-pressure phase ICM3, owing to the lack of INS data for $P < 4$ GPa. Further INS experiments under high pressures are required.

V. CONCLUSIONS

We investigated the magnetic interactions under high-pressure conditions for the frustrated triangular-lattice antiferromagnet CFO through ND and INS experiments. In the ND experiments, we found that the $H_{||c}$-induced phase transition from CM1 to ICM2 at H_{c1}

was significantly suppressed by the application of pressure. In contrast, the phase transition from ICM2 to CM2 at H_{c2} did not change with the application of pressure. We also observed that the magnetic ordering of the ICM3 phase was not affected by $H_{||c}$ up to 10 T. In the INS experiment, we observed a change in the excitation energy at the energy minimum and the zone boundary in the spin-wave dispersion relation. Comparing the experimental results with the spin-wave calculations revealed that the change in spin-wave excitation can be explained by the reduction in either the uniaxial anisotropy term or the degree of separation in the nearest-neighbor exchange interactions.

Acknowledgements

We acknowledge the STFC for providing the neutron beamtime. Raw data were obtained from https://doi.org/10.5286/ISIS.E.RB1610350. The neutron scattering experiments in JRR-3 were conducted as a joint research project at the Institute for Solid State Physics, University of Tokyo (Nos. 21801, 21929, and 22802). This work was supported by JSPS KAKENHI grants (Nos. 17KK0099, 19H04400, 22H00297).

---

[1] M. Matsuda, M. Takeda, M. Nakamura, K. Kakurai, A. Oosawa, E. Lelievre-Berna, J.-H. Chung, H. Ueda, H. Takagi, and S.-H. Lee, Spiral spin structure in the Heisenberg pyrochlore magnet $CdCr_2O_4$, Phys. Rev. B **75**, 104415 (2007).

[2] Nirmal J. Ghimire, Rebecca L. Dally, L. Poudel, D. C. Jones, D. Michel, N. Thapa Magar, M. Bleuel, Michael A. McGuire, J. S. Jiang, J. F. Mitchell, Jeffrey W. Lynn, and I. I. Mazin, Competing magnetic phases and fluctuation-driven scalar spin chirality in the kagome metal YMn_6Sn_6, Sci. Adv. **6**, eabe2680 (2020).

[3] A. P. Ramirez, A. Hayashi, R. J. Cava, R. Siddharthan and B. S. Shastry, Zero-point entropy in 'spin ice', Nature **399**, 333 (1999).

[4] S. T. Bramwell and M. J. P. Gingras, Spin ice state in frustrated magnetic pyrochlore materials, Science, **294**, 16 (2001).

[5] T. Okubo, S. Chung, and H. Kawamura, Multiple–q States and the Skyrmion Lattice of the Triangular-Lattice Heisenberg Antiferromagnet under Magnetic Fields, Phys. Rev. Lett. **108**,

017206 (2012).

[6] J. A. M. Paddison, B. K. Rai, A. F. May, S. Calder, M. B. Stone, M. D. Frontzek, and A. D. Christianson, Magnetic Interactions of the Centrosymmetric Skyrmion Material, Phys. Rev. Lett. **129**, 137202 (2022).

[7] T. Itou, A. Oyamada, S. Maegawa and R. Kato, Nat. Phys. **6** 673 (2010). Instability of a quantum spin liquid in an organic triangular-lattice antiferromagnet,

[8] J. A. M. Paddison, M. Daum, Z. Dun, G. Ehlers, Y. Liu, M. B. Stone, H. Zhou and M. Mourigal Continuous excitations of the triangular-lattice quantum spin liquid $YbMgGaO_4$, Nat. Phys. **13** 117 (2017).

[9] I. A. Sergienko, C. Sen, and E. Dagotto, Ferroelectricity in the Magnetic E–Phase of Orthorhombic Perovskites, Phys. Rev. Lett. **97**, 227204 (2006).

[10] M. Mostovoy, Ferroelectricity in Spiral Magnets, Phys. Rev. Lett. **96**, 067601 (2006).

[11] T. A. Kaplan and S. D. Mahanti, Canted-spin-caused electric dipoles: A local symmetry theory, Phys. Rev. B **83**, 174432 (2011).

[12] T. Kimura, T. Goto, H. Shintani, K. Ishizaka, T. Arima, and Y. Tokura, Magnetic control of ferroelectric polarization, Nature **426**, 55 (2003).

[13] S.-W. Cheong and M. Mostovoy, Multiferroics: a magnetic twist for ferroelectricity, Nature Mater. **6**, 13 (2007).

[14] K. Penc, N. Shannon, and H. Shiba, Half-Magnetization Plateau Stabilized by Structural Distortion in the Antiferromagnetic Heisenberg Model on a Pyrochlore Lattice, Phys. Rev. Lett. **93**, 197203 (2004).

[15] H Ueda, H. A. Katori, H. Mitamura, T. Goto, H. Takagi, Magnetic-Field Induced Transition to the 1/2 Magnetization Plateau State in the Geometrically Frustrated Magnet $CdCr_2O_4$, Phys. Rev. Lett. **94**, 047202 (2005).

[16] N. Terada, D. D. Khalyavin, P. Manuel, T. Osakabe, P. G. Radaelli and H. Kitazawa, Pressure-induced polar phases in multiferroic delafossite $CuFeO_2$, Phys. Rev. B **89**, 220403(R) (2014).

[17] N. Terada, N. Qureshi, L. C. Chapon and T. Osakabe, Spherical neutron polarimetry under high pressure for a multiferroic delafossite ferrite, Nat. Commun. **9**, 4368 (2018).

[18] H. Takatsu, S. Yonezawa, S. Fujimoto, and Y. Maeno, Unconventional Anomalous Hall Effect in the Metallic Triangular-Lattice Magnet, Phys. Rev. Lett. **105**, 137201 (2010).

[19] N. Terada, D. D. Khalyavin, P. Manuel, Y. Tsujimoto, K. Knight, P. G. Radaelli, H. S. Suzuki,

and H. Kitazawa, Spiral-Spin-Driven Ferroelectricity in a Multiferroic Delafossite $AgFeO_2$, Phys. Rev. Lett. **109**, 097203 (2012).

[20] M. Frontzek, G. Ehlers, A. Podlesnyak, H. Cao, M. Matsuda, O. Zaharko, N. Aliouane, S. Barilo and S. V. Shiryaev, Magnetic structure of $CuCeO_2$: a single crystal neutron diffraction study J. Phys.: Condens. Matter **24** 016004 (2012).

[21] S. Mitsuda, H. Yoshizawa, N. Yaguchi, and M. Mekata, Neutron diffraction study of $CuFeO_2$, J. Phys. Soc. Jpn. **60**, 1885 (1991).

[22] M. Mekata, N. Yaguchi, T. Takagi, T. Sugino, S. Mitsuda, H. Yoshizawa, N. Hosoito, T. Shinjo, Successive Magnetic Ordering in $CuFeO_2$–A New Type of Partially Disordered Phase in a Triangular Lattice Antiferromagnet– J. Phys. Soc. Jpn. **62**, 4474 (1993).

[23] S. Mitsuda, N. Kasahara, T. Uno, and M. Mase, Partially Disordered Phase in Frustrated Triangular Lattice Antiferromagnet $CuFeO_2$, J. Phys. Soc. Jpn. **67**, 4026 (1998).

[24] T. Nakajima, S. Mitsuda, S. Kanetsuki, K. Tanaka, K. Fujii, N. Terada, M. Soda, M. Matsuura, and K. Hirota, Electric polarization induced by a proper helical magnetic ordering in a delafossite multiferroic $CuFe_{1-x}Al_AlO_2$, Phys. Rev. B **77**, 052401 (2008).

[25] T. Nakajima, S. Mitsuda, K. Takahashi, M. Yamano, K. Masuda, H. Yamazaki, K. Prokes, K. Kiefer, S. Gerischer, N. Terada, H. Kitazawa, M. Matsuda, K. Kakurai, H. Kimura, Y. Noda, M. Soda, M. Matsuura, and K. Hirota, Comprehensive study on ferroelectricity induced by a proper-screw-type magnetic ordering in multiferroic $CuFeO_2$: Nonmagnetic impurity effect on magnetic and ferroelectric order, Phys. Rev. B **79**, 214423 (2009).

[26] F. Ye, J. A. Fernandez-Baca, R. S. Fishman, Y. Ren, H. J. Kang, Y. Qiu, and T. Kimura, Magnetic Interactions in the Geometrically Frustrated Triangular Lattice Antiferromagnet $CuFeO_2$ Phys. Rev. Lett. **99**, 157201 (2007).

[27] T. Nakajima, A. Suno, S. Mitsuda, N. Terada, S. Kimura, K. Kaneko and H. Yamauchi, Magnons and electromagnons in a spin-lattice-coupled frustrated magnet $CuFeO_2$ as seen via inelastic neutron scattering, Phys. Rev. B **84**, 184401 (2011).

[28] S. Kimura, T. Fujita, N. Nishihagi, H. Yamaguchi, T. Kashiwagi, M. Hagiwara, N. Terada, Y. Sawai, and K. Kindo, Multifrequency ESR measurements of the triangular lattice antiferromagnet $CuFeO_2$ in high magnetic fields, Phys. Rev. B **84**, 104449 (2011).

[29] L. C. Chapon, P. Manuel, P. G. Radaelli, C. Benson, L. Perrott, S. Ansell, N. J. Rhodes, D. Raspino, D. Duxbury, E. Spill and J. Norris, Wish: The new powder and single crystal magnetic

diffractometer on the second target station, *Neutron News* **22**, 22 (2011).

[30] T. Osakabe, K. Kuwahara, D. Kawana, K. Iwasa, D. Kikuchi, Y. Aoki, M. Kohgi, and H. Sato, Pressure-Induced Antiferromagnetic Order in Filled Skutterudite $PrFe_4P_{12}$ Studied by Single-Crystal High-Pressure Neutron Diffraction J. Phys. Soc. Jpn. **79**, 034711 (2010).

[31] H. Yamauchi, T. Osakabe, E. Matsuoka, and H. Onodera, Pressure Effects on Quadrupolar and Magnetic Ordering in HoB_2C_2 Observed by Single-Crystal Neutron Diffraction, J. Phys. Soc. Jpn. **81**, 034715 (2012).

[32] N. Terada, Development of Hybrid-Anvil-Cell for Polarized and Unpolarized Neutron Diffraction Study, Trans. Mater. Res. Soc. Jpn. **44**, 1-5 (2019).

[33] Y. Ajiro, T. Asano, T. Takagi, M. Mekata, H. A. Katori and T. Goto, High-field magnetization process in the triangular lattice antiferromagnet $CuFeO_2$ up to 100 T, Physica B **201**, 71 (1994).

[34] S. Mitsuda, M. Mase, K. Prokes, H. Kitazawa, and H. A. Katori, Field-Induced Magnetic Phase Transitions in a Triangular Lattice Antiferromagnet $CuFeO_2$ up to 14.5 T, J. Phys. Soc. Jpn. **69**, 3513 (2000).

[35] O. A. Petrenko, G. Balakrishnan, M. R. Lees, D. McK. Paul, and A. Hoser, High-magnetic-field behavior of the triangular-lattice antiferromagnet $CuFeO_2$, Phys. Rev. B **62**, 8983 (2000).

[36] T. T. A. Lummen, C. Strohm, H. Rakoto, and P. H. M. van Loosdrecht, Mapping the magnetic phase diagram of the frustrated metamagnet $CuFeO_2$, Phys. Rev. B **81**, 224420 (2010).

[37] See Supplemental Material

[38] N. Terada, S. Mitsuda, H. Ohsumi, and K. Tajima, "Spin-Driven" Crystal Lattice Distortion in Frustrated Magnet $CuFeO_2$: Synchrotron X-ray Diffraction Study, J. Phys. Soc. Jpn. **75**, 023602 (2006).

[39] F. Ye, Y. Ren, Q. Huang, J. A. Fernandez-Baca, P. Dai, J. W. Lynn, and T. Kimura, Spontaneous spin-lattice coupling in the geometrically frustrated triangular lattice antiferromagnet $CuFeO_2$, Phys. Rev. B **73**, 220404(R) (2006).

[40] N. Terada, Y. Tanaka, Y. Tabata, K. Katsumata, A. Kikkawa, and S. Mitsuda, Restoring higher symmetric crystal structure with magnetic field in triangular lattice antiferromagnet $CuFeO_2$, J. Phys. Soc. Jpn. **75**, 113702 (2006).

[41] N. Terada, Y. Narumi, Y. Sawai, K. Katsumata, U. Staub, Y. Tanaka, A. Kikkawa, T. Fukui, K. Kindo, T. Yamamoto, R. Kanmuri, M. Hagiwara, H. Toyokawa, T. Ishikawa, and H. Kitamura, Correlation between crystal structure and magnetism in the frustrated antiferromagnet $CuFeO_2$

under high magnetic fields Phys. Rev. B **75**, 224411 (2007).

[42] N. Terada, S. Mitsuda, Y. Tanaka, Y. Tabata, K. Katsumata, and A. Kikkawa, Field-induced Incommensurate Lattice Modulations in the Delafossite $CuFeO_2$, J. Phys. Soc. Jpn. **77**, 054701 (2008).

[43] R. S. Fishman and S. Okamoto, Noncollinear magnetic phases of a triangular-lattice antiferromagnet and of doped $CuFeO_2$, Phys. Rev. B **81**, 020402(R) (2010).

[44] J. T. Haraldsen and R. S. Fishman, Effect of interlayer interactions and lattice distortions on the magnetic ground state and spin dynamics of a geometrically frustrated triangular-lattice antiferromagnet, Phys. Rev. B **82**, 144441 (2010).

[45] J. T. Haraldsen, F. Ye, R. S. Fishman, J. A. Fernandez-Baca, Y. Yamaguchi, K. Kimura, and T. Kimura, Multiferroic phase of doped delafossite $CuFeO_2$ identified using inelastic neutron scattering, Phys. Rev. B **82**, 020404 (2010).

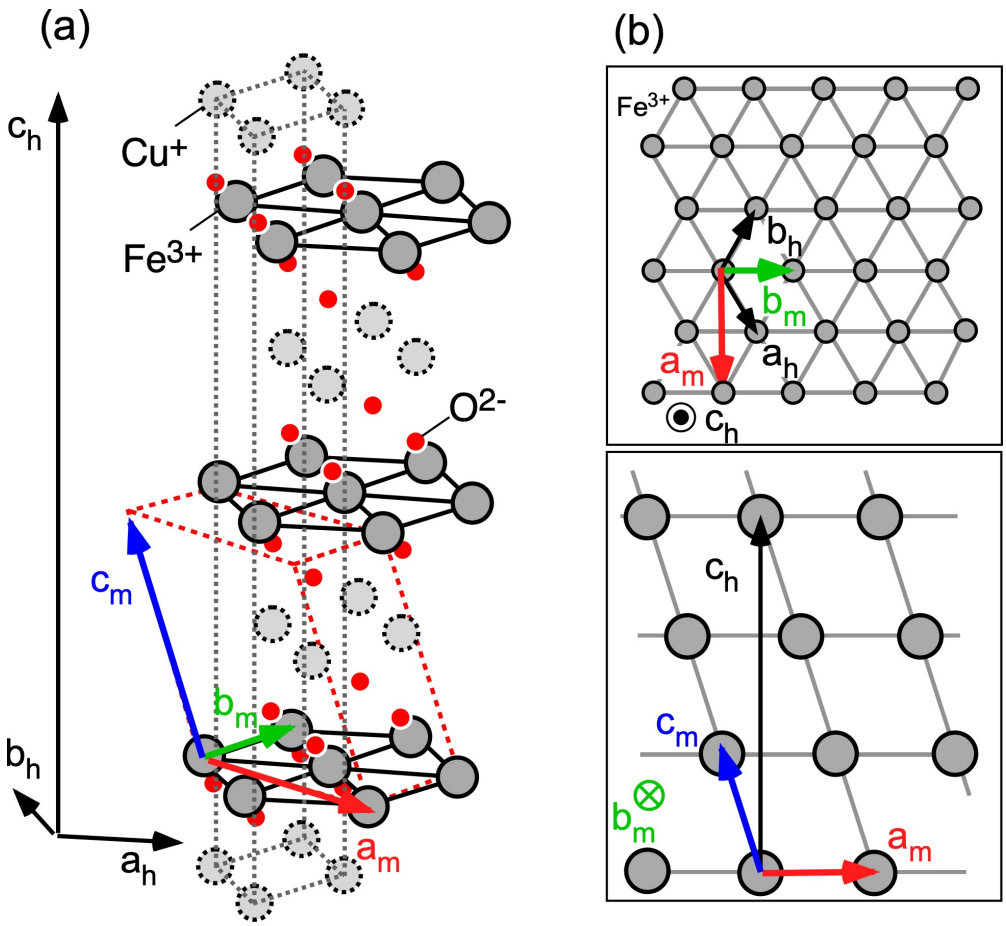

FIG. 1: (a)Crystal structure of $CuFeO_2$. Dotted lines denote hexagonal and monoclinic unit cells. (b)The relationship between the hexagonal and monoclinic basis vectors ($a_m = a_h - b_h$, $b_m = a_h + b_h$, $c_h = (-a_h + b_h + c_h)/3$, where Fe is at the origin).

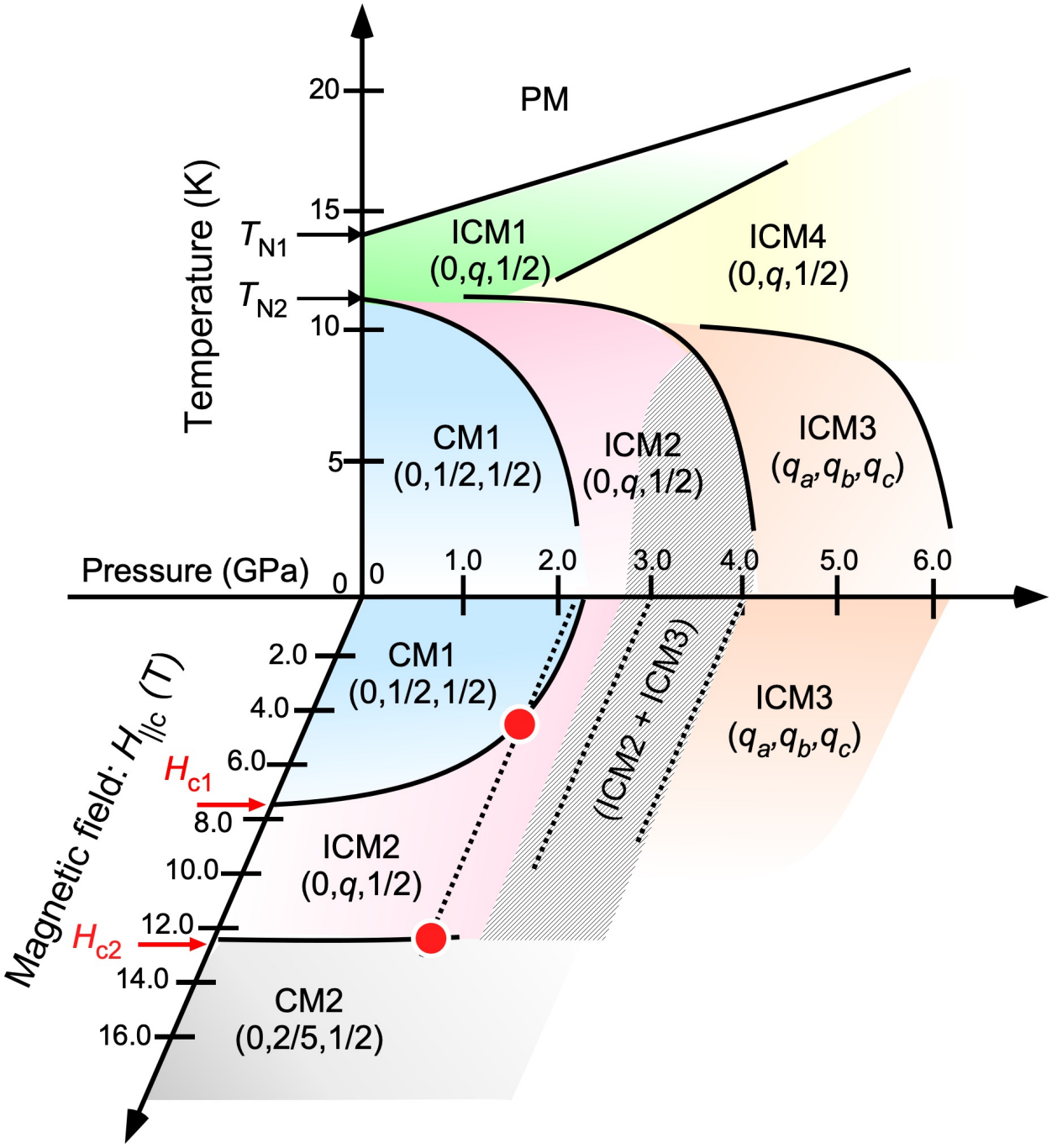

FIG. 2: Schematic illustration of the magnetic phase diagram of $CuFeO_2$ as functions of temperature, pressure and magnetic field along the hexagonal c axis. The temperature versus pressure phase diagram was taken from previous work[17]. The solid lines and the solid circles denote the phase boundaries and the points where the phase transitions were found in the present study. The dotted line show the magnetic field that we have investigated in this study. The hatched area denote the coexistence region of ICM2 and ICM3 phases.

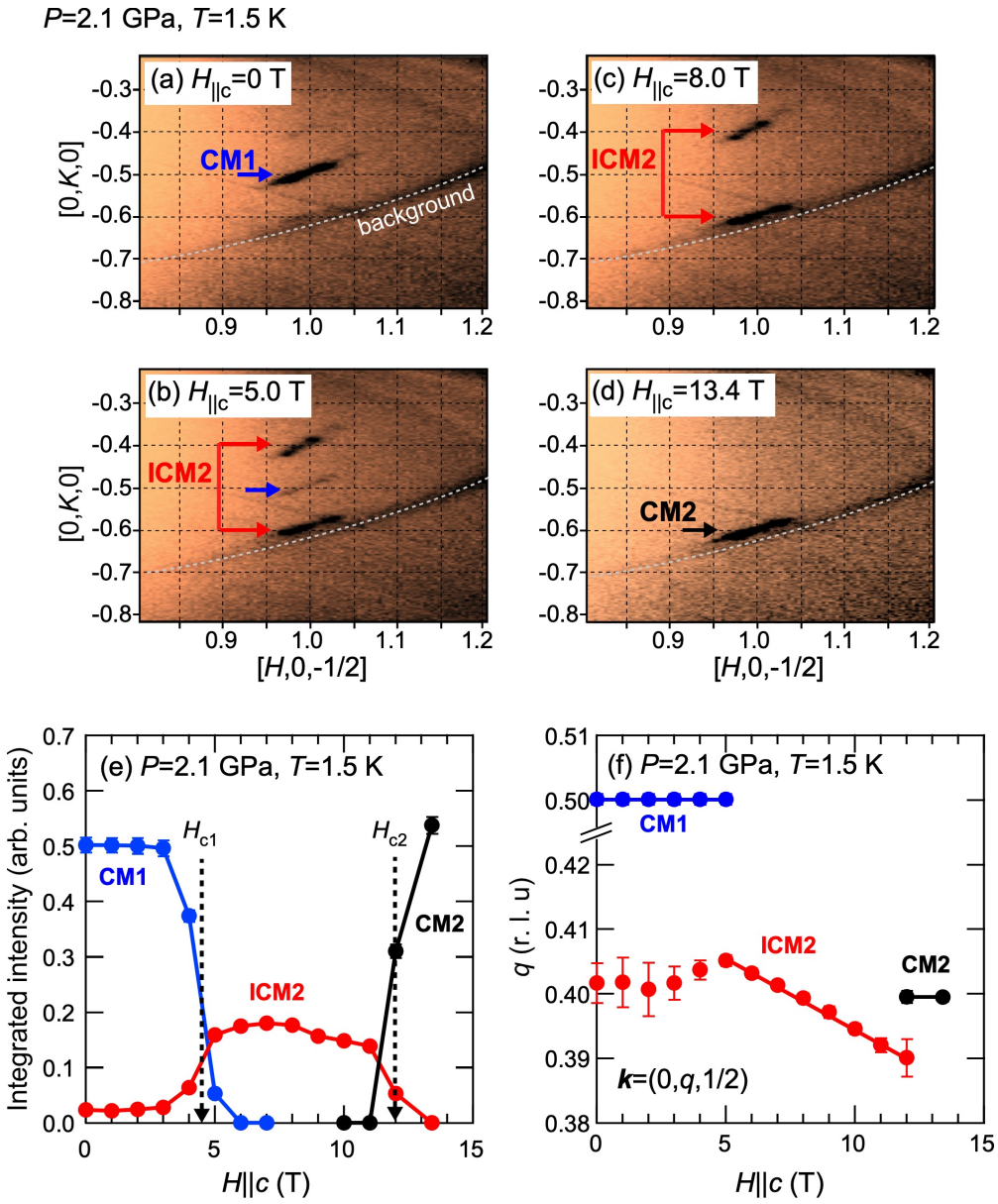

FIG. 3: Neutron diffraction intensity images measured at typical magnetic fields along the hexagonal c axis, ($H_{||c}$) (a)$H_{||c} = 0$ T, (b) $H_{||c} = 5.0$ T, (c) $H_{||c} = 8.0$ T and (d) $H_{||c} = 13.4$ T for $T = 1.5$ K and P=2.1 GPa. $H_{||c}$ dependence of (e)integrated intensity of the magnetic Bragg reflection at $\boldsymbol{Q} = (1, q, -\frac{1}{2})$ and (f) magnetic propagation wave number q at $T = 1.5$ K and P=2.1 GPa.

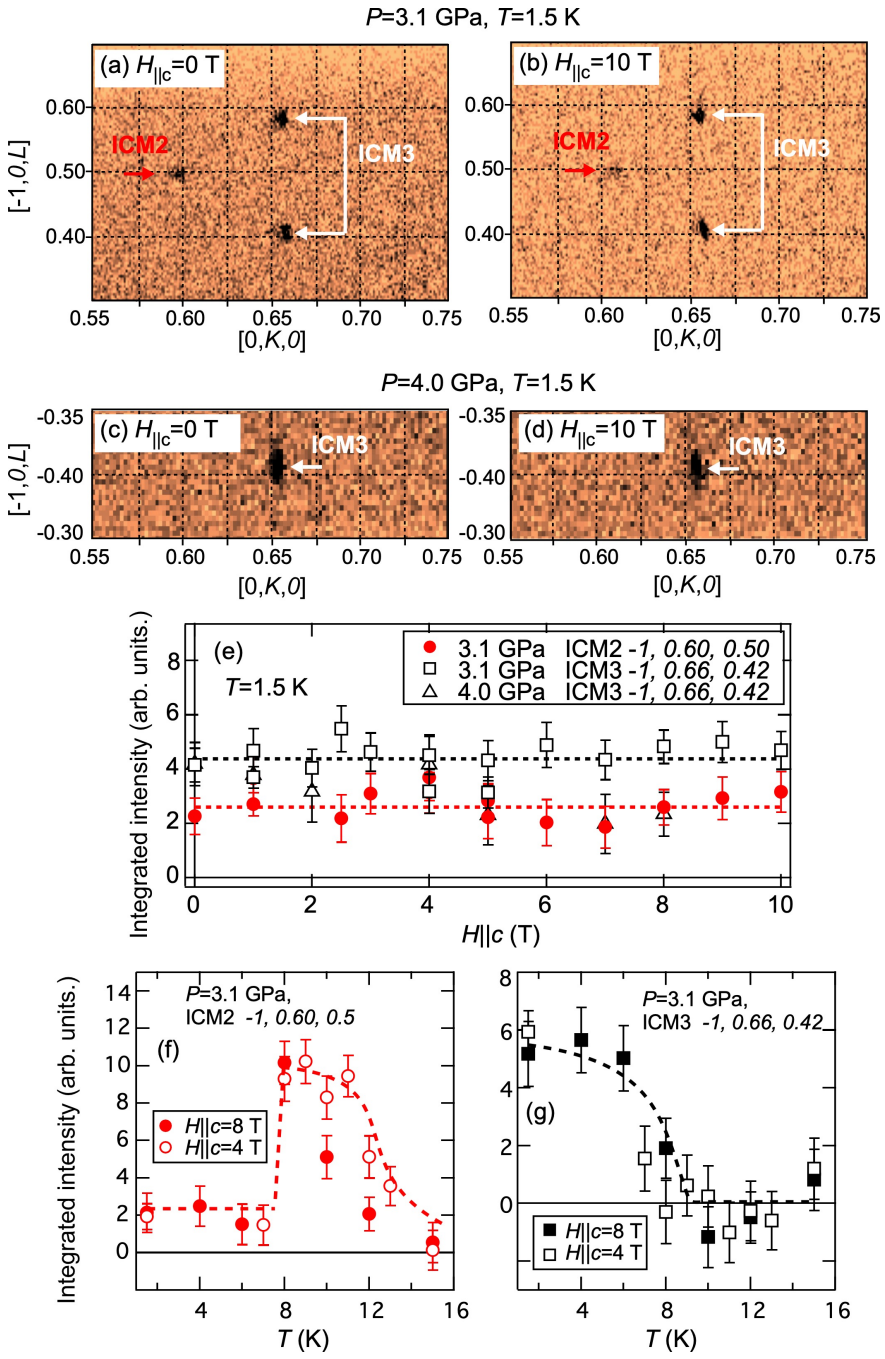

FIG. 4: Neutron diffraction intensity images measured at typical magnetic fields along the hexagonal c axis, ($H_{||c}$) and pressures at T =1.5 K, (a)$H_{||c} = 0$ T and (b)$H_{||c} = 10$ T at P =3.1 GPa, and (c)$H_{||c} = 0$ T and (b)$H_{||c} = 10$ T at P =4.0 GPa. (e)$H_{||c}$ dependence of the integrated intensities corresponding to ICM2 and ICM3 phases at 3.1 GPa nad 4.0 GPa at $T = 1.5$ K. Temperature dependence of the integrated intensities corresponding to (f) ICM2 and (g) ICM3 phases at $H_{||c} = 4$ T and 8 T and $P = 3.1$ GPa.

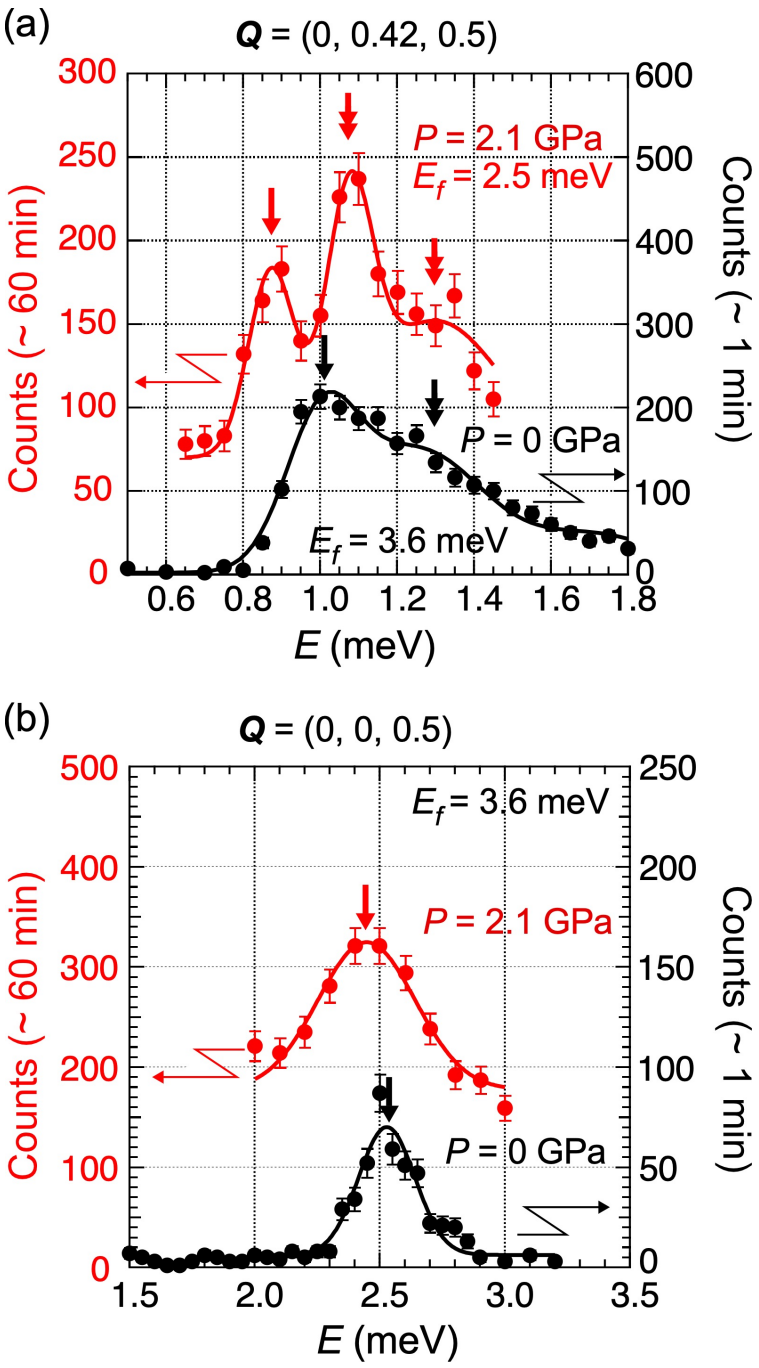

FIG. 5: Energy dependence of neutron intensity for the constant-Q scans at (a) Q-position where the spin-wave dispersion shows the minimum ($\boldsymbol{Q} = (0, 0.42, 0.5)$), and (b) the magnetic zone boundary ($\boldsymbol{Q} = (0, 0, 0.5)$). These data were measured with HER spectrometer. The data at ambient pressure were measured without the pressure cell, which were taken from Ref.[27].

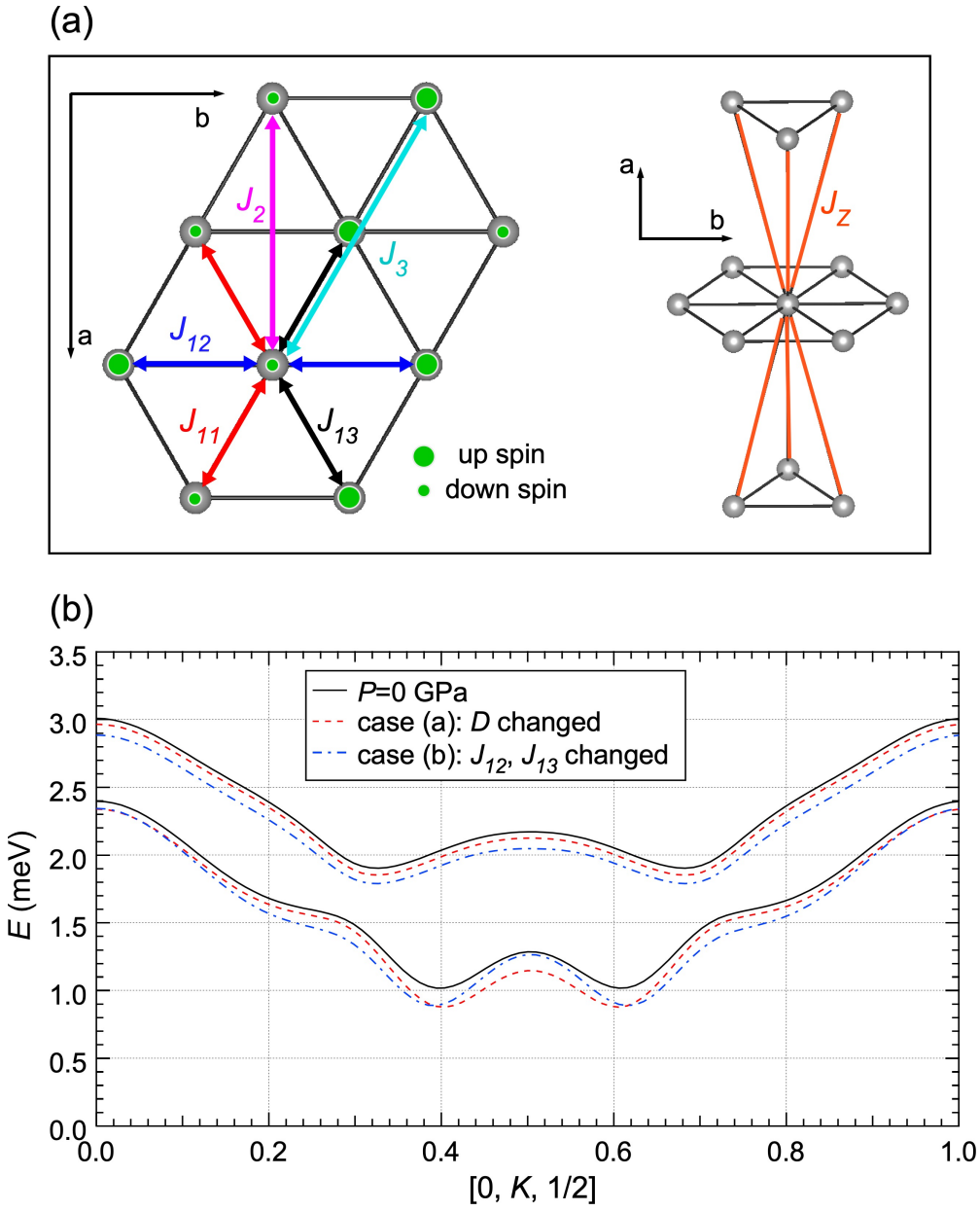

FIG. 6: (a)The exchanged paths considered in the present study. (b)The calculated spin wave dispersion relation at ambient pressure (solid line)[27]. The dispersion curves denoted by dotted and broken lines were calculated with the uniaxial anisotropy parameter, D, and J_{12} (and J_{13}), which are changed from the ambient pressure values, respectively. The details are described in the main text.

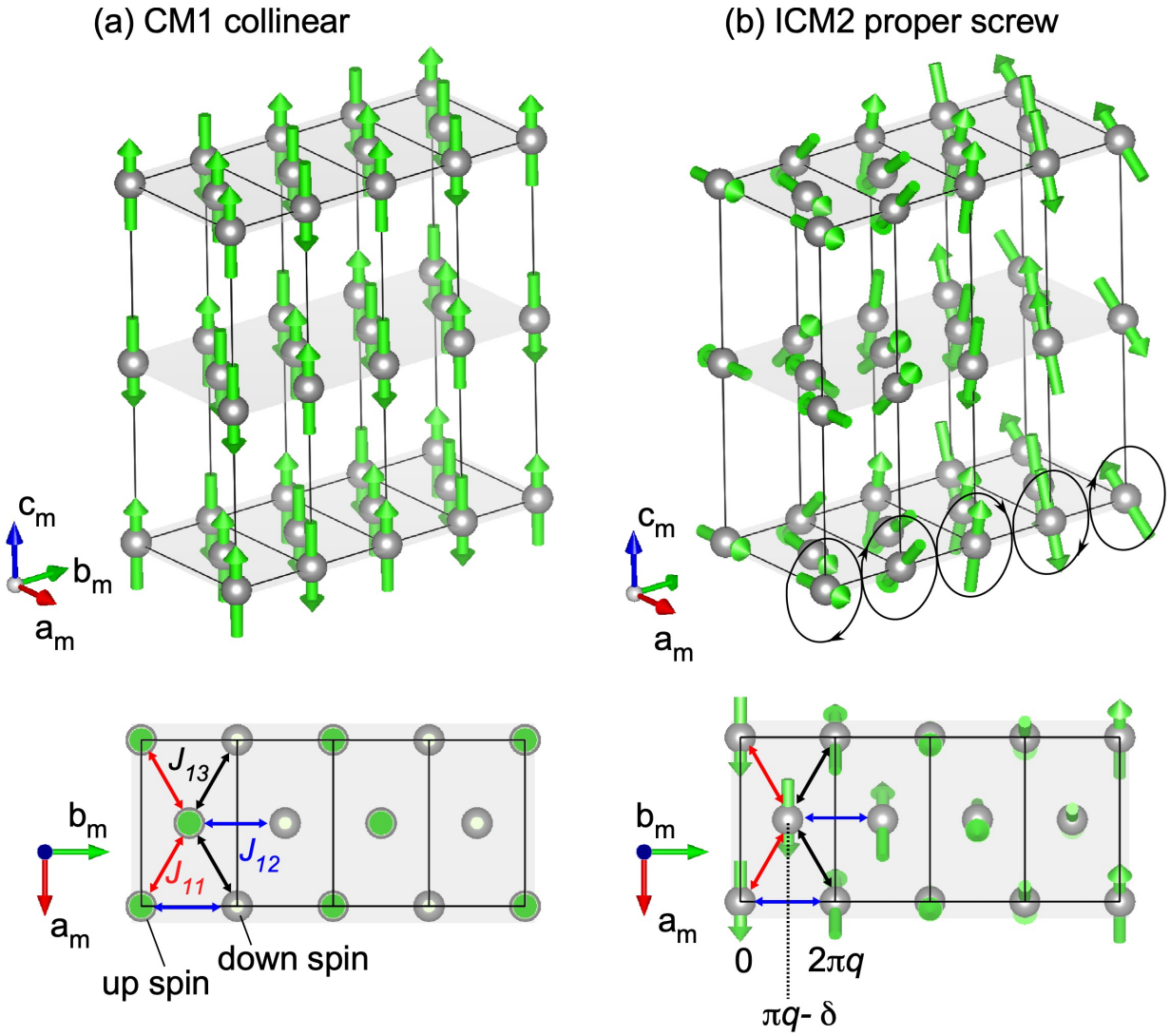

FIG. 7: Schematic illustrations of magnetic structures for (a) collinear structure of CM1 and (b) proper screw structure of ICM2 phase.